

Neural Shadow Art

Caoliwen Wang

University of Science and Technology of China
China
wclw1021@mail.ustc.edu.cn

Bailin Deng

School of Computer Science and Informatics at Cardiff
University
the United Kingdom
DengB3@cardiff.ac.uk

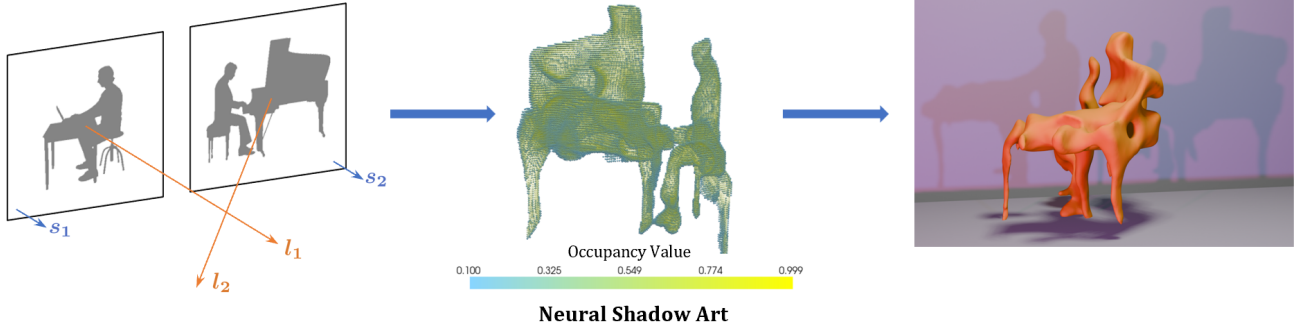


Figure 1: We introduce Neural Shadow Art, which leverages implicit function representations to offer new possibilities for Shadow Art.

ABSTRACT

Shadow art is a captivating form of sculptural expression, where the projection of a sculpture in a specific direction reveals a desired shape with high accuracy. In this work, we introduce Neural Shadow Art, which leverages implicit function representations to expand the possibilities of shadow art. Our method provides a more flexible framework that allows projections to match input binary images under various lighting directions and screen orientations, without requiring the light source to be perpendicular to the screen. Unlike previous approaches, our method permits rigid transformations of the projected geometry relative to the input binary image. By optimizing lighting directions and screen orientations simultaneously through the implicit representation of 3D models, we ensure the projection closely resembles the target image. Additionally, like prior works, our method accommodates specific angular constraints, allowing users to fix the projection angle when necessary. Beyond its artistic significance, our approach proves valuable for industrial applications, demonstrating lower material usage and enhanced geometric smoothness. This capability avoids oversimplified results, such as the intersection of cylindrical volumes formed by light rays and the projection image. Furthermore, our approach excels in generating sculptures with complex topologies, surpassing previous methods and achieving sculptural effects akin to those in contemporary art.

Permission to make digital or hard copies of all or part of this work for personal or classroom use is granted without fee provided that copies are not made or distributed for profit or commercial advantage and that copies bear this notice and the full citation on the first page. Copyrights for third-party components of this work must be honored. For all other uses, contact the owner/author(s).
© 2024 Copyright held by the owner/author(s).

CCS CONCEPTS

• **Computing methodologies** → **Shape modeling**; *Rendering*; • **Applied computing** → **Fine arts**.

KEYWORDS

Shadow Art, Shape modeling, Implicit representations

1 INTRODUCTION

Shadow art is a unique form of artistic expression that uses shadows as the medium of representation. Many artists have skillfully created intricate geometric structures and light fields to project images, utilizing spatial projections of objects to convey artistic visions. Historically, there have been numerous captivating exhibitions of shadow art. For example, Tim Noble and Sue Webster assembled everyday objects into seemingly random three-dimensional structures, but when illuminated from specific directions, these structures cast highly detailed and lifelike shadows. Figure 2a illustrates a profile of a human face, while Figure 2b depicts two people sitting back-to-back. In Figure 2c, the artists simulated a cityscape at sunrise, where the warm-toned light field creates the illusion of a recognizable scene. These artist-created works rely on the precise spatial arrangement of materials to produce visually striking patterns on a screen under illumination from specific directions. However, this process demands exceptional spatial reasoning skills, particularly when the desired images need to be projected from multiple directions, as achieving the intended artistic effect through intuition alone becomes exceedingly challenging. Therefore, a relatively generalizable algorithm is essential for the artistic design of shadow art. Figure 2d shows the cover of Douglas Hofstadter’s book *Gödel, Escher, Bach*, featuring geometric structures that, when viewed from three orthogonal directions, cast shadows



Figure 2: (a)-(c): Examples of historically renowned shadow art created by artists, where carefully positioning materials produced artistic effects in the projection from a specific direction. (d)-(f): Shadow art pieces showcasing distinct artistic information under varying lighting conditions and projection plane orientations, representing the definition of shadow art as conceived by the vision and graphics community.

forming the letters G, E and B. Further examples of shadow art include Figure 2e, which is derived from [Mitra and Pauly 2009], the pioneering work in shadow art. It demonstrates the projection of a complex geometric structure along three non-orthogonal directions. Figure 2f is derived from [Schwartzburg and Pauly 2012], where a geometric sculpture projects two distinct silhouettes—one of a figure preparing to throw an object and another holding a torch aloft—demonstrating remarkable artistic expression through careful shadow manipulation.

These examples of shadow art are both engaging and thought-provoking, exemplifying the precise calculation and control of light and three-dimensional geometry. In computer graphics, shadow art can be considered an inverse problem of shadow generation. Instead of generating shadows from a known scene, shadow art algorithms take as input a desired shadow image to compute the corresponding three-dimensional geometry that will cast the intended shadows. This process requires sophisticated geometric optimization and manipulation to produce aesthetically compelling and technically accurate results.

Mitra and Pauly were the first to introduce shadow art to the visual and graphics community, formally addressing the problem through an explicit geometric optimization method [Mitra and Pauly 2009]. However, we approach this problem by formulating it as solving the implicit occupancy function of the geometric sculpture, from which the final geometric mesh is extracted.

In the overall pipeline, we leveraged the powerful fitting ability of neural implicit expressions of 3D geometry. In addition to using the differentiable rendering technique to approximate the input images, we allowed for rigid deformation of the input images. We also implemented a joint optimization of lighting angles, projection plane orientation, and geometric smoothness. This extended the possibilities of shadow art, making the resulting artistic effects more vivid and better meeting users’ strict demands for shadow effects. Furthermore, we penalized the volume of the geometry, which not only better meets the industrial requirement of minimizing material usage, but also aligns with the goal of shadow art as an art form—achieving the desired shadow effect with less material. Solutions that approximate simple intersections like the one formed by the direction of light and projection into a cylinder do not fully capture the artistic charm of shadow art.

Contributions: The main contributions of this paper are:

- We provide a new representation of shadow art, making this art form more flexible. Unlike earlier works, our approach is not constrained to having the light direction always perpendicular to the projection plane.
- We support rigid transformations of the input image and joint optimization of the light direction and projection plane orientation, ensuring that the projection results from our model closely resemble the input, especially when the input images own complex topologies.

- We incorporate geometric smoothness and volume optimization into our model, enabling the use of less material. This not only meets industrial production requirements but also highlights the intricacy and elegance of this art form.

2 RELATED WORKS

This section introduces related work in the fields of computer graphics and computer vision that is relevant to our research.

Shadow information. Many works have analyzed the information that can be extracted from shadows and applied it to tasks such as shape reconstruction or generation. Waltz was the first to use shadows to infer the 3D shape in line drawings [Waltz 1975]. Building on this work, Steven and Kanade developed a method that uses a collection of shadows to infer the surface orientations of both polyhedra and curved surfaces [Shafer and Kanade 1983]. Bouguet and Perona proposed a method based on a "weak structured lighting" system, which extracts the 3D shape of objects by observing the spatial and temporal locations of the shadows cast [Bouguet and Perona 1999]. Savarese et al. proposed a reconstruction system for recovering the shape of objects through silhouettes and shadow carving, demonstrating the unique information embedded in shadows, such as in the discovery of the concavities of objects [Savarese et al. 2007]. In recent years, many studies have also leveraged deep learning techniques to learn information from shadows, applying them to reconstruction or generation tasks. Kushagra et al. have explored learning implicit representations of entire scenes from shadow information based on volume rendering [Tiwary et al. 2022]. Ruoshi et al. leveraged generative models to predict the 3D geometry of objects using shadows, achieving promising results, particularly in scenarios where the objects to be reconstructed are partially or completely occluded [Liu et al. 2023]. These advancements collectively highlight the evolving role of shadows in extracting and refining 3D structural information in computer vision.

Shadow art. To date, numerous works have been conducted in the field of shadow art. The shadow art problem was first introduced by Mitra and Pauly, who proposed an explicit voxel-based optimization method. Their work aimed at constructing 3D geometries that produce specific projections from given viewpoints [Mitra and Pauly 2009]. However, due to the use of As-Rigid-As-Possible (ARAP) deformation during the optimization process, the resulting projection often undergoes excessive deformation compared to the input. This is typically undesirable for users, especially when the input image has a more complex topology, as it can significantly impact the visual quality. In addition, Sadekar et al. introduced a differentiable rendering framework that achieves the same objective. They further demonstrated that this approach can be extended to other artistic forms, such as geometry prediction from half-toned face images, highlighting the broader applicability of their method in artistic rendering and geometric reconstruction tasks [Sadekar et al. 2022]. However, since the method does not process the input images, the result may be poor when the input images have inconsistent configurations. In addition, the output meshes often exhibit unexpected flips and prominent spikes, which negatively impact the visual quality. Moreover, their methods, particularly the

mesh-based approaches, do not perform well when handling inputs with complex topologies.

In addition to the shadow art effect we have implemented, there are other artistic expressions utilizing shadows. Min et al. presented a novel shadow art algorithm that generates grayscale shadows using an area light (or an array of point lights) and occluding objects, expanding the scope of light sources [Min et al. 2017]. Hsiao et al. presented an algorithm for creating multi-view wire sculptures, where the projections of these wire sculptures from different directions are represented by specified line information [Hsiao et al. 2018]. In recent years, there has been growing interest in the manufacturability of such art forms. Tojo et al. developed a comprehensive workflow for fabricating wire art from various input types and proposed a 3D-printable jig structure to produce the generated wire paths [Tojo et al. 2024]. Further artistic work is discussed in Wu et al.'s review on 3D visual optical art design [Wu et al. 2022].

Representations for 3D learning. Learning-based 3D reconstruction approaches can be broadly categorized into voxel-based, point cloud-based, mesh-based, and implicit representation-based methods.

Voxel-based methods [Brock et al. 2016; Maturana and Scherer 2015; Sharma et al. 2016; Wu et al. 2015] are direct extension of 2D pixel representation and is one of the most straightforward approaches. However, even with very sparse data, the resolution is constrained and cannot be excessively high [Tatarchenko et al. 2017]. An increase in resolution results in a substantial rise in storage requirements. Point cloud-based methods [Klokov and Lempitsky 2017; Qi et al. 2017; Ruizhongtai Qi et al. 2016; Yang et al. 2018] are more memory-efficient but lack topological information, often requiring intensive post-processing. Mesh-based methods, on the other hand, do not require post-processing but learning methods have not been readily extended to such irregular representations. Such data usually suffer from noise, missing data and resolution problems such as [Cosmo et al. 2016].

However, implicit representations of geometry circumvent the aforementioned issues and are becoming increasingly prevalent in learning-based research. Park et al. proposed storing 3D geometry by training Signed Distance Field (SDF), which significantly reduces storage requirements while preserving complex topologies, and also demonstrated its potential in completion tasks [Park et al. 2019]. Mescheder et al. employed occupancy networks for implicit representation of geometry, extending the original binary occupancy to continuous values in the range $[0,1]$, and demonstrated the network's strong capabilities in both supervised and unsupervised learning [Mescheder et al. 2019]. These two works present the two most common geometric representations in the current field of 3D geometry learning: Signed Distance Field (SDF) and occupancy. Mildenhall et al. made significant advancements in multi-view synthesis by inputting 3D points and visual information of the observation direction into a neural network to obtain color and volumetric occupancy [Mildenhall et al. 2021]. Wang et al., building on NeRF-based work, trained Signed Distance Field (SDF) representations for reconstructing objects based on volumetric rendering errors [Wang et al. 2021]. Long et al. extended similar approaches to unsigned distance functions, thereby broadening the types of reconstructed surfaces to include non-closed surfaces

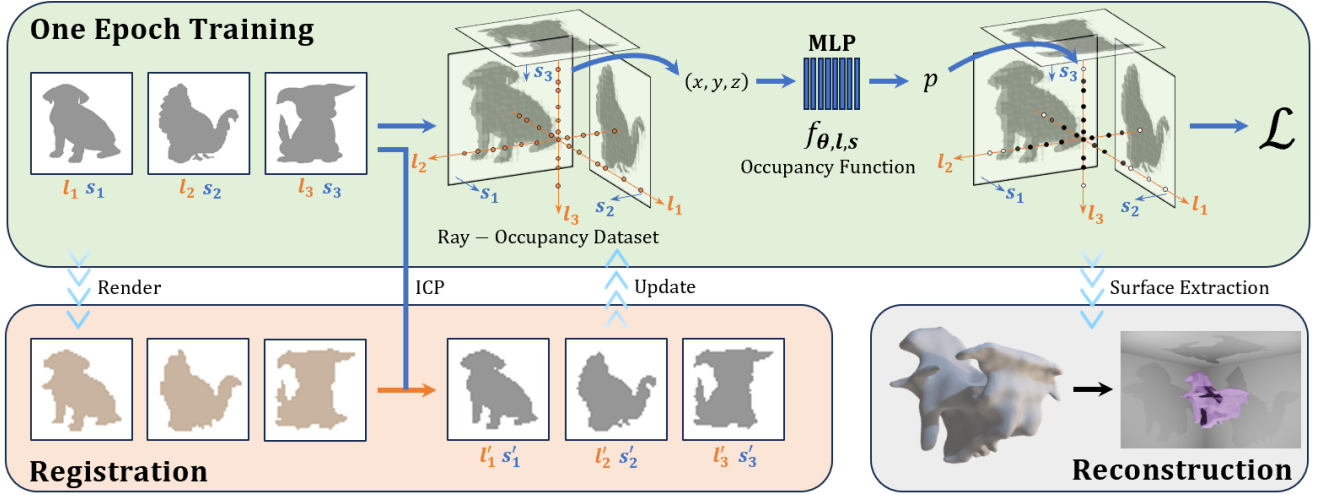


Figure 3: Overall workflow of our method. (a) In each epoch, we first generate the Ray-Occupancy dataset based on the input, compute the loss, and update the occupancy function using backpropagation. (b) At the end of each epoch, the result is rendered, and the input image is updated by performing ICP between the rendered result and the input image. Additionally, l_i and s_i are updated for the next epoch. (c) The surface is extracted and simulated using the implicit function.

[Long et al. 2023]. Signed distance functions are currently being widely utilized; however, to our knowledge, there has been no work on geometric volume measurement using signed distance functions. Our work shares similarities with these works in terms of the neural network training approach. However, our goal is to generate geometric shapes rather than synthesizing novel view images, which allows us to use a less complex neural network. Additionally, we represent objects using occupancy instead of distance field.

3 METHOD

3.1 Occupancy Function

We first define a 3D-to-1D neural occupancy function $f_{\theta, l, s}$ based on sparse binary images.

$$f_{\theta, l, s} : \mathbb{R}^3 \rightarrow [0, 1], \quad f_{\theta, l, s}(x, y, z) = p \in [0, 1]. \quad (1)$$

Here, θ denotes the parameters of the neural network, $l \in \mathbb{R}^3$ represents the direction vector of the ray from object to eyes, and $s \in \mathbb{R}^3$ denotes the normal vector of the projection plane pointing towards the object. We assume that both l and s are normalized and according to their definition, $\cos\langle l, s \rangle > 0$. In this expression, the input is the coordinates of a point in 3D space, and the output is a probability occupancy value in the range $[0, 1]$. A value of 0 indicates that the point is unoccupied, while values closer to 1 indicate a higher probability that the point is occupied. In our framework, values greater than $\tau = 0.1$ are typically considered occupied. This definition is inconsistent with that proposed by [Mescheder et al. 2019], where their definition takes the viewing angle as part of the input, whereas ours only relies on 3D coordinates.

We utilize an MLP network to fit the occupancy function $f_{\theta, l, s}$ defined in Equation (1), which predicts the occupancy value for each 3D coordinate in the normalized space. To ensure the model

performs well even at low input image resolutions, the $[x, y, z]$ coordinates are normalized and constrained within the range $[-0.5, 0.5]$. The architecture of our network is similar to that of [Mildenhall et al. 2021]. For any coordinate p in the input 3D coordinates, positional encoding $\gamma(p)$ is first applied, followed by fitting with an MLP network $f'_{\theta, l, s}$.

$$\gamma(p) = \left(p, \sin(2^0 p), \cos(2^0 p), \dots, \sin(2^{L-1} p), \cos(2^{L-1} p) \right) \quad (2)$$

$$f_{\theta, l, s} = f'_{\theta, l, s} \circ \gamma \quad (3)$$

Here, L relates to the dimension of positional coding. In fitting $f'_{\theta, l, s}$, we employ eight fully connected layers, each using ReLU activations and 256 channels per layer. To ensure the output values are within the range $[0, 1]$, the activation function of the final layer is a sigmoid function.

3.2 One Epoch Training

"Ray-Occupancy" dataset. Before one epoch training, we generate a "Ray-Occupancy" dataset based on the light direction parameter l , the normal vector of the projection plane s and corresponding binary images. Assuming that the light direction corresponding to a projection constraint is l_0 and the normal vector of the projection plane is s_0 , the ray's starting position generate at the pixel (r, c) in the image can be calculated as:

$$r_s = \frac{-dl_0}{\cos\langle l_0, s_0 \rangle} + \left(\frac{r}{h} - \frac{1}{2} \right) r + \frac{w}{h} \left(\frac{c}{w} - \frac{1}{2} \right) c \quad (4)$$

$$r_e = r_s + \frac{2dl_0}{\cos\langle l_0, s_0 \rangle} \quad (5)$$

Here, r_s and r_e represent the start and end points of the ray, respectively. d denotes the distance from the center of the projection plane to the origin in the normalized space, which is set to 0.5 in

our framework to correspond with the range of the positional coordinates. h and w represent the height and width of the input image, respectively. \mathbf{r} and \mathbf{c} are uniquely determined by \mathbf{s}_0 , as expressed in the following equation:

$$\mathbf{c} = \begin{cases} \frac{(-s_0[1], s_0[0], 0)}{\|(-s_0[1], s_0[0], 0)\|_2} & \text{if } \mathbf{s}_0 \neq (0, 0, 1) \\ [0, 1, 0] & \text{if } \mathbf{s}_0 = (0, 0, 1) \end{cases} \quad (6)$$

$$\mathbf{r} = \mathbf{c} \times \mathbf{s}_0 \quad (7)$$

When using Equation (4), (5), (6), and (7) for calculations, the imaging position can be finely adjusted, which facilitates the gradient propagation of \mathbf{l} and \mathbf{s} . Then the rays are discretized and stored as random points within n (can be adjusted) equally spaced segments. The quantities described above are visualized in Figure 4.

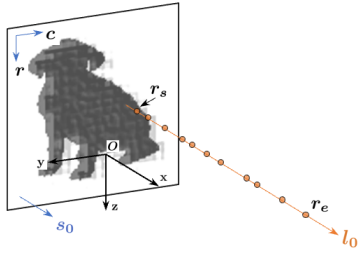


Figure 4: Visualization of the quantities in Equation (4), (5), (6), (7), illustrating the process of calculating the "Ray-Occupancy" dataset.

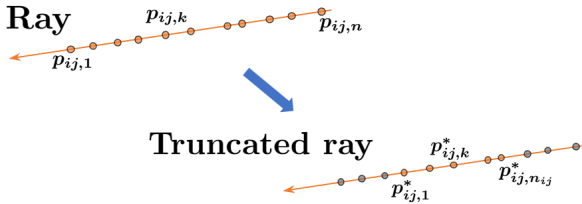


Figure 5: Visualization of the quantities in Equation (9), demonstrating the truncation process of a given ray. The gray points represent the truncated points.

In the "Ray-Occupancy" dataset, occupancy represents the actual occupancy value of the ray: if the relative position on the image is black, it is considered occupied with an occupancy value of 1; if the position is white, it is considered unoccupied with an occupancy value of 0.

Rendering loss. We first propose a core image error to ensure that the reconstructed geometry satisfies the projection constraints as closely as possible. We estimate the error between the actual projection and the predicted projection by using the actual occupancy values along the rays and the predicted occupancy probabilities.

For the i th batch \mathcal{B} ,

$$\mathcal{L}_{ren} = \text{MSE}(\mathbf{M}_i, \mathbf{O}_i), \quad (8)$$

Here, \mathbf{M}_i represents the true occupancy value vector for all rays in one batch, \mathbf{O}_i represents the estimated occupancy value vector for all rays in one batch and is computed as follows:

$$O_{ij} = 1 - \prod_{k=1}^{n_{ij}} (1 - f(\mathbf{p}_{ij,k}^*)), \quad j = 1, 2, \dots, |\mathcal{B}|. \quad (9)$$

Here, O_{ij} represents the j th value of \mathbf{O}_i , let the number of the sampling points within the truncated region for the j th ray in the i th batch be n_{ij} , and the set of points in truncated ray be $\{\mathbf{p}_{ij,k}^*\}_{k=1}^{n_{ij}}$. The set is visualized in Figure 5. For the defined "Ray-Occupancy" dataset, the sampled points of a ray under one shadow constraint may not lie within the cylindrical volume formed by another shadow constraint. This discrepancy can result in inconsistencies during computation, where a ray contributes to one shadow constraint but not to another. To address this issue, we apply truncation to the rays, constraining them to a specific bounded region. In our experiments, we use a cubic region of $[-0.5, 0.5]^3$ or a sphere with a radius of 0.5 according to the input direction. This choice is due to the surface extraction process from the implicit function, where we first compute the values on the grid points within $[-0.5, 0.5]^3$ and subsequently apply the marching cubes algorithm [Lorensen and Cline 1987]. In addition to applying truncation, input images with a white border of a certain thickness can also mitigate the adverse effects of this issue.

This expression fully provides the degree of freedom for determining whether a point on a ray is occupied, enabling the shadow art to satisfy projection constraints in other directions. Since the predicted occupancy probability O_{ij} defined in 9 approaches 1 if at least one sampling point on the ray has an occupancy value close to 1, and only approaches 0 when the occupancy values of all sampling points on the ray are close to 0, it highlights the relationship between point-wise occupancy and ray-wise occupancy. Each point holds the same significance, making this expression unbiased.

Geometry losses. We should minimize the amount of surface intersections on a given ray; otherwise, multiple layers of parallel structures may occur. Therefore, we propose the first geometry loss, shown in Equation (10), which estimates the difference in function values between adjacent points along the same ray.

$$\mathcal{L}_{geo1} = \frac{1}{|\mathcal{B}|} \sum_j \frac{1}{n} \sum_{k=1}^{n-1} (f(\mathbf{p}_{ij,k+1}) - f(\mathbf{p}_{ij,k}))^2. \quad (10)$$

In addition, we aim for the resulting geometric surface to be relatively smooth. Since our training is ray-based, we first need to determine which sampling points along the ray are located on the surface. According to the definition of $f_{\theta, \mathbf{l}, \mathbf{s}}$ in 3.1, we know that the gradient $\|\nabla f_{\theta, \mathbf{l}, \mathbf{s}}\|_2$ of points on the surface is significantly larger than that of points inside or outside the surface. Therefore, we use the following inequality as the criterion for determining whether a point \mathbf{p}_0 is on the surface:

$$\|\nabla f_{\theta, \mathbf{l}, \mathbf{s}}(\mathbf{p}_0)\|_2 > \alpha w. \quad (11)$$

Here, w has the same definition as before, and α is a threshold control parameter used for decision-making. In our experiments, $\alpha = 0.4$. $w = \frac{1}{w}$ represents the direction of the directional derivative of $f_{\theta, \mathbf{l}, \mathbf{s}}$ for discrete sampling points with a spacing of $\frac{1}{w}$ in the

direction connecting two points. Under the influence of α , this can be used to determine surface points.

We cannot directly use the backpropagation of the neural network to estimate $\nabla f_{\theta, l, s}(\mathbf{p}_0)$, as the neural network may exhibit drastic changes at scales smaller than the sampling scale $\frac{1}{w}$. However, at nearby discrete sampling points, the predicted occupancy values are roughly the same. In this case, the result from backpropagation leads to a very large gradient estimate, while in fact, this should not be classified as a surface. On the contrary, we estimate $\nabla f_{\theta, l, s}(\mathbf{p}_0)$ using the neighborhood of the sampling point in three-dimensional space. Let \mathbf{p}_i be a point in the neighborhood. Corresponding to 11, we use the first-order finite difference to estimate $\nabla f_{\theta, l, s}(\mathbf{p}_0)$:

$$\nabla f_{\theta, l, s}(\mathbf{p}_0) \cdot (\mathbf{p}_i - \mathbf{p}_0) = f_{\theta, l, s}(\mathbf{p}_i) - f_{\theta, l, s}(\mathbf{p}_0). \quad (12)$$

Let the matrix $\mathbf{K} \in \mathbb{R}^{k_1 \times 3}$ represent the arrangement of the k_1 neighboring points in rows, and let the vector $\mathbf{b} \in \mathbb{R}^{k_1}$ represent the row-wise arrangement of the differences $f_{\theta, l, s}(\mathbf{p}_i) - f_{\theta, l, s}(\mathbf{p}_0)$. In our experiment, $k_1 = 26$, representing all the neighbor cubes. We solve the following least squares equation to estimate $\nabla f_{\theta, l, s}(\mathbf{p}_0)$:

$$\mathbf{K} \nabla f_{\theta, l, s}(\mathbf{p}_0) = \mathbf{b}. \quad (13)$$

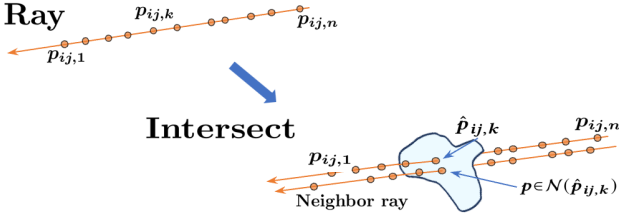


Figure 6: Visualization of the quantities in Equation 14, demonstrating how to find k_2 nearest points based on neighbor rays.

For the j th ray in the i th batch, let the number of surface points be \hat{n}_{ij} , and the set of surface points be $\{\hat{\mathbf{p}}_{ij,k}\}_{k=1}^{\hat{n}_{ij}}$. The set is visualized in Figure 6. We penalize the surface smoothness using the following formula:

$$\mathcal{L}_{geo2} = \frac{1}{|\mathcal{B}|} \sum_j \frac{1}{\hat{n}_{ij}} \sum_{k=1}^{\hat{n}_{ij}} \frac{1}{|\mathcal{N}(\hat{\mathbf{p}}_{ij,k})|} \sum_{\mathbf{p} \in \mathcal{N}(\hat{\mathbf{p}}_{ij,k})} \frac{|\nabla f_{\theta, l, s}(\hat{\mathbf{p}}_{ij,k}) - \nabla f_{\theta, l, s}(\mathbf{p})|}{\|\hat{\mathbf{p}}_{ij,k} - \mathbf{p}\|_2}. \quad (14)$$

Here, $\mathcal{N}(\hat{\mathbf{p}}_{ij,k})$ represents the nearest k_2 neighborhood of $\hat{\mathbf{p}}_{ij,k}$ on the surface, satisfying the condition in 11, and $|\cdot|$ denotes the l_1 -norm of a vector, which optimizes the sparsity of the surface point differences within the neighborhood. $\mathcal{N}(\hat{\mathbf{p}}_{ij,k})$ can be calculated by the intersection of neighbor rays (from neighbor pixel) and surface, which is visualized in Figure 6. The calculation of $\nabla f_{\theta, l, s}(\mathbf{p})$ can be derived according to 13. In our experiments, $k_2 = 6$.

Volume loss. we introduce a volume loss, shown in (15), which employs a soft counting method to estimate a value that is approximately positively correlated with the volume of the reconstructed geometry. This soft counting method maps occupancy

values greater than the threshold τ to values close to 1, and occupancy values less than τ to values close to 0, where T is an adjustable temperature parameter.

$$\mathcal{L}_{vol} = \frac{1}{|\mathcal{B}|} \sum_j \sum_{k=1}^{n_{ij}} \frac{\omega_{ij,k}}{1 + \exp(-\frac{f(\mathbf{p}_{ij,k}^*) - \tau}{T})}. \quad (15)$$

$$\omega_{ij,k} = \begin{cases} \|\mathbf{p}_{ij,2}^* - \mathbf{p}_{ij,1}^*\|_2 & \text{if } k = 1, \\ \|\mathbf{p}_{ij,n_{ij}}^* - \mathbf{p}_{ij,n_{ij}-1}^*\|_2 & \text{if } k = n_{ij}, \\ \frac{1}{2} \|\mathbf{p}_{ij,k}^* - \mathbf{p}_{ij,k-1}^*\|_2 + \frac{1}{2} \|\mathbf{p}_{ij,k}^* - \mathbf{p}_{ij,k+1}^*\|_2 & \text{otherwise.} \end{cases} \quad (16)$$

Here, The weight $w_{ij,k}$ quantifies the region influenced by each discrete sampling point. Owing to the uniform sampling of rays on the image, this formulation directly correlates to the estimation of the geometric volume.

Regulation loss. The outcomes of model should also converge to either 0 or 1 values, to make sure we are not introducing a capability for the network to use transparency as a valid asset to reduce the rendering loss. Therefore, we use a regulation loss, which is shown in (17).

$$\mathcal{L}_{reg} = \frac{1}{|\mathcal{B}|} \sum_{j=1}^{|\mathcal{B}|} \frac{1}{n} \sum_{k=1}^n \min \left(f^2(\mathbf{s}_{ij,k}), (1 - f(\mathbf{s}_{ij,k}))^2 \right). \quad (17)$$

The final loss over one batch is shown:

$$\mathcal{L} = \beta \mathcal{L}_{ren} + \beta_1 \mathcal{L}_{geo1} + \beta_2 \mathcal{L}_{geo2} + \beta_3 \mathcal{L}_{vol} + \beta_4 \mathcal{L}_{reg}. \quad (18)$$

Here, β represents the maximum value of the quotient obtained by dividing the size of each input image by the bounding kernel of the occupied region, which is used to better penalize the projection image's accuracy; $\beta_1, \beta_2, \beta_3$, and β_4 are adjustable parameters. Specifically, we set $\beta_1 = 10^{-3} \times 2^{\min(\text{epoch}, 3)}$, $\beta_2 = 10^{-4} \times (1 \text{ if } \text{epoch} > 3 \text{ else } 0)$, $\beta_3 = 10^{-4} \times (1 \text{ if } \text{epoch} > 3 \text{ else } 0)$, and $\beta_4 = 5 \times 10^{-2} \times 2^{\min(\text{epoch}, 3)}$. The weights for β_1 and β_4 are increased during training to accelerate model convergence. On the other hand, β_2 and β_3 are not trained initially, as the geometry has not yet been sufficiently formed at that stage. We use the Adam solver to optimize the model, ultimately reconstructing a relatively optimal geometry.

3.3 Training

In Section 3.2, we introduce the training process for a single epoch, which preserves the gradients of \mathbf{l} and \mathbf{s} , allowing for joint optimization throughout the overall training process. Our framework also allows for fixing the ray direction and the receiving screen normal, as in previous work [Mitra and Pauly 2009; Sadkar et al. 2022]; or it allows for optimizing either one of them.

Moreover, our framework accommodates rigid deformation of the projection map. Specifically, after every five epochs, we visualize the current projection map, extract the boundary point cloud, and similarly extract the boundary point cloud from the input projection map. The two point clouds are then aligned using the Iterative Closest Point (ICP) algorithm [Besl and McKay 1992], and the resulting rigid transformation is applied to the original projection figure to generate a new projection figure. Training proceeds with

the updated figure in the subsequent epoch. This operation is not performed after every epoch due to the fact that training within a single epoch does not sufficiently refine the input projection.

3.4 Reconstruction

In Section 3.3, we obtained an occupancy network representation of the geometry. To extract the surface geometry from this implicit representation, we employ the well-established marching cubes algorithm [Lorensen and Cline 1987].

4 RESULTS

To evaluate our approach, we first compare it with previous methods (Figure 7, Table 1). Our method demonstrates competitive performance across all tests. Specifically, [Mitra and Pauly 2009] exhibits excessive deformation compared to the input image due to its use of the ARAP algorithm. In contrast, the voxel-based method in [Sadekar et al. 2022] introduces floating artifacts and abrupt short lines that affect the shadow quality, while the mesh-based method in [Sadekar et al. 2022] generates sharp, sheet-like meshes with significant flipping. In comparison, our model produces relatively smooth surface geometries that more closely align with the input image.

Table 1 quantifies the projection results of different methods in terms of their similarity to the original image under rigid transformations, using IOU and DS metrics. Our approach achieves the best performance in both metrics. Furthermore, Figure 7 illustrates that our model occupies relatively smaller volumes, whereas methods like [Mitra and Pauly 2009; Sadekar et al. 2022] exhibit intersecting geometric cylinders.

Figure 8 demonstrates the advantages of our results in geometric consistency. It clearly shows that previous mesh-based methods exhibit significant flips in the output geometry.

Figure 9 shows how our work introduces more possibilities for the original shadow art. For inputs with complex topology, the deformation in [Mitra and Pauly 2009] is more severe, and [Sadekar et al. 2022] produces unstable geometry, while our method generates accurate and geometrically stable results. The second row presents results not addressed by previous works. We demonstrate two different projections on the same projection plane, utilizing the non-orthogonality between the light rays and the projection plane. A slight angle optimization significantly improves the fit to the projection constraints. Similarly, this structure provides new inspiration for artistic creation.

As our output generates watertight meshes, the results are compatible with current 3D printing technologies. Some manufactured physical examples are shown in Figure 10. This further validates the accuracy of our method in fitting shadows.

Compared to previous works, the advantages of our model are summarized in Table 2. Compatibility resolution refers to handling cases where no geometry satisfies the input constraints. In [Mitra and Pauly 2009], an As-Rigid-As-Possible (ARAP) transformation was applied, often causing significant distortions in the projection compared to the input. [Sadekar et al. 2022], however, did not address compatibility issues. Light and screen optimization were also neglected in prior works, both assuming a perpendicular relationship between the light screen and light rays by default. Regarding

complex topologies, [Mitra and Pauly 2009] handles certain cases partially but introduces distortions due to large ARAP deformations. In contrast, the voxel optimization approach in [Sadekar et al. 2022] produces floating regions and non-watertight results due to insufficient geometric constraints. The mesh optimization method in [Sadekar et al. 2022] struggles with complex topologies, often causing excessive mesh flips, as the initial state is a sphere, and the optimization process remains topologically equivalent to the sphere, unable to resolve different topologies. Finally, volume optimization, crucial for manufacturing, was not addressed in either of the previous works.

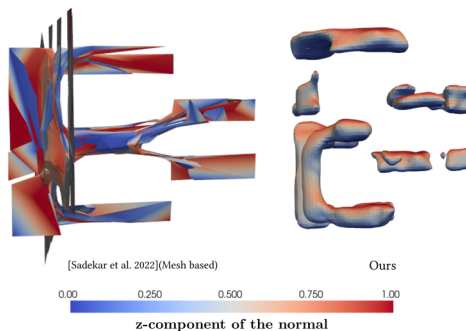


Figure 8: Visualization of the normal vector, highlighting the geometric consistency of the geometry in our results.

5 CONCLUSION

In this work, we give an implicit representation of shadow art, expanding its potential beyond the traditional art form. Our method produces geometries that are more consistent with projection constraints including complex topologies, using less material while maintaining superior geometric properties. It also allows optimization of both the light and screen angles, enabling the fitting of non-compatible input images and removing the restriction that the light must be perpendicular to the projection plane. Our approach excels in above properties, and we introduce a surface geometric smoothing technique for this 3D representation.

However, there are still some limitations. Our method requires precise 2D projection images as input and does not yet support auxiliary input formats such as guided language, which could be valuable for artistic design. Additionally, when the input image contains intricate details, the ray-based nature of our method, which relies on pixel-level computations, may result in longer computation times. Finally, in cases where the generated geometry is disconnected, we address this by using short rods to connect the geometry or place the geometry within a defined space and fill the remaining volume with translucent materials. While this approach is not straightforward in 3D printing due to potential breakage during the removal of supports, the advantage of using short rods lies in their minimal impact on the overall projection. During light rendering, soft shadow effects cause the projection of the rods to become blurry when viewed from a distance, thereby limiting their influence on the final projection results.

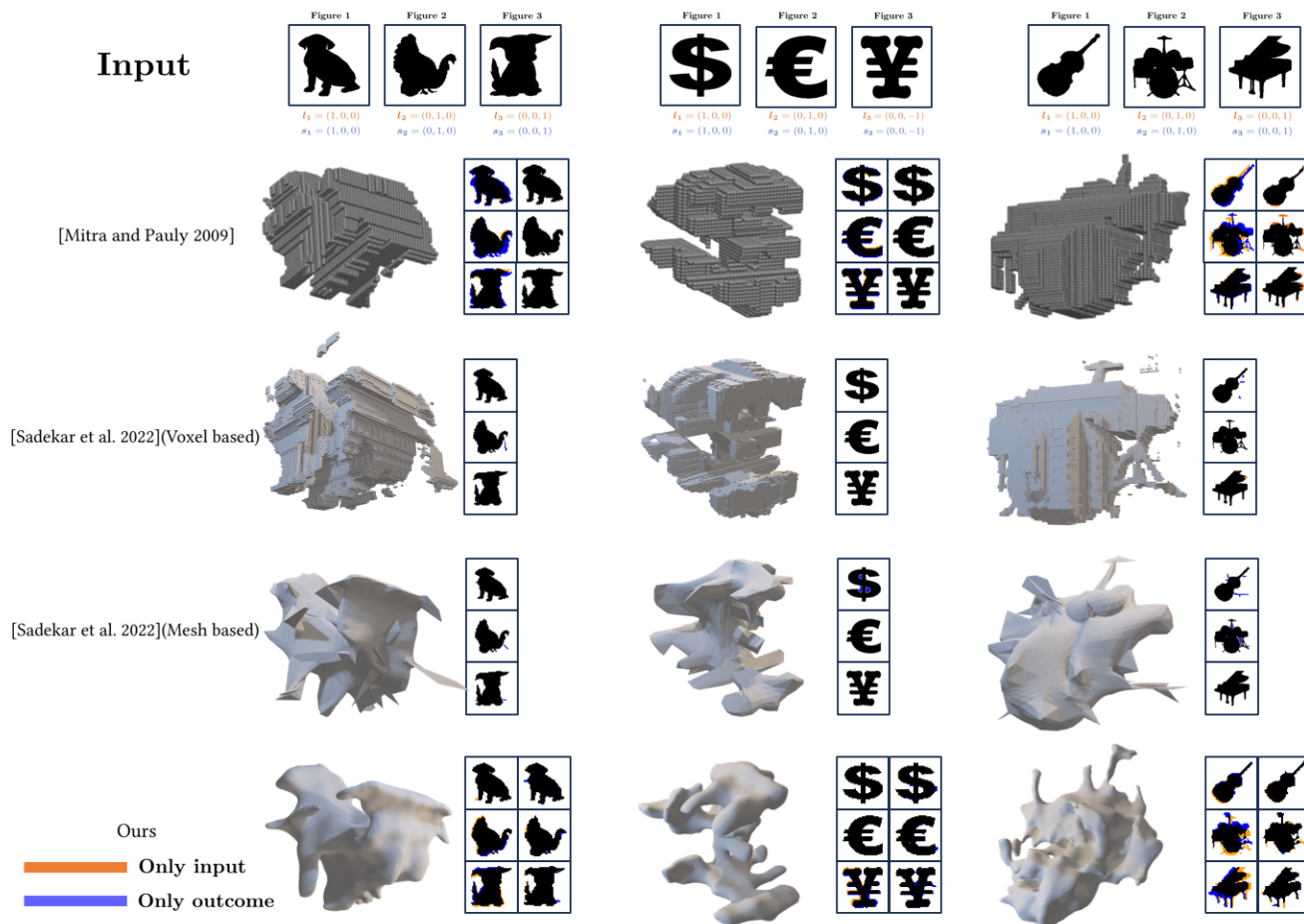


Figure 7: Comparison with prior works. For [Mitra and Pauly 2009], the first column shows input vs. deformed target projection, and the second shows deformed target vs. final projection. For [Sadekar et al. 2022], the column represents input vs. final projection without deformation. For ours, the first column shows input vs. rigid registration, and the second shows rigid registration vs. final projection.

Method	Animal		Currency		Music	
	IOU	DS	IOU	DS	IOU	DS
Shadow Art [Mitra and Pauly 2009]	0.8227	0.9027	0.8665	0.9285	0.7496	0.8532
Shadow Art Revisited [Sadekar et al. 2022] (Voxel-based)	0.8756	0.9336	0.9160	0.9561	0.9008	0.9478
Shadow Art Revisited [Sadekar et al. 2022] (Mesh-based)	0.8474	0.9174	0.8695	0.9299	0.8528	0.9204
Ours	0.9671	0.9833	0.9606	0.9799	0.9521	0.9754

Table 1: Comparison of accuracy with the original image. Our comparison focuses on the alignment between the output projection and the input projection after rigid registration.

REFERENCES

- Paul J. Besl and Neil D. McKay. 1992. A Method for Registration of 3-D Shapes. *IEEE Transactions on Pattern Analysis and Machine Intelligence* 14, 2 (1992), 239–256. <https://doi.org/10.1109/34.121791>
- Jean-Yves Bouguet and Pietro Perona. 1999. 3D Photography Using Shadows in Dual-Space Geometry. *Int. J. Comput. Vision* 35, 2 (Nov. 1999), 129–149. <https://doi.org/10.1023/A:1008124523456>
- André Brock, Theodore Lim, James M. Ritchie, and Nick Weston. 2016. Generative and Discriminative Voxel Modeling with Convolutional Neural Networks. *CoRR* abs/1608.04236 (2016). <http://arxiv.org/abs/1608.04236>
- Luca Cosmo, Emanuele Rodolà, Michael Bronstein, Andrea Torsello, Daniel Cremers, and Yusuf Sahillioğlu. 2016. SHREC’16: Partial Matching of Deformable Shapes. <https://doi.org/10.2312/3dor.20161089>
- Kai-Wen Hsiao, Jia-Bin Huang, and Hung-Kuo Chu. 2018. Multi-view wire art. *ACM Trans. Graph.* 37, 6, Article 242 (dec 2018), 11 pages. <https://doi.org/10.1145/3272127.3275070>
- Roman Klokov and Victor Lempitsky. 2017. Escape from Cells: Deep Kd-Networks for the Recognition of 3D Point Cloud Models. In *2017 IEEE International Conference on Computer Vision (ICCV)*. 863–872. <https://doi.org/10.1109/ICCV.2017.99>

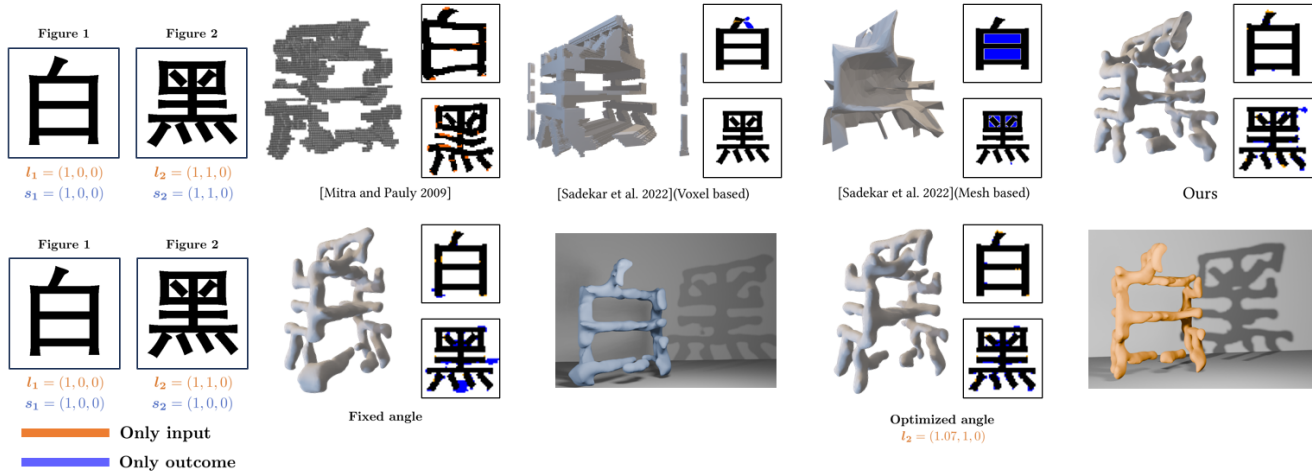


Figure 9: More possibilities. First row: projection plane orthogonal to light rays. Second row: projection plane not orthogonal to light rays, a scenario not handled by prior methods. (2/5) result without angle optimization; (4/5) result with angle optimization, slight angle change improves fit; (3/5) and (5/5) corresponding projection simulation.



Figure 10: Fabricated results, demonstrating the precision of the shadows and the smoothness of the geometry. (3/3) is beyond the capabilities of previous works.

Method	Compatibility resolution	Light and screen optimization	Complex topology	Volume Optimization
Shadow Art[Mitra and Pauly 2009]	✓	×	×	×
Shadow Art Revisited[Sadekar et al. 2022](Voxel based)	×	×	✓	×
Shadow Art Revisited[Sadekar et al. 2022](Mesh based)	×	×	×	×
Ours	✓	✓	✓	✓

Table 2: The advantages of our model, compared with previous work.

R. Liu, S. Menon, C. Mao, D. Park, S. Stent, and C. Vondrick. 2023. What You Can Reconstruct from a Shadow. In *2023 IEEE/CVF Conference on Computer Vision and Pattern Recognition (CVPR)*. IEEE Computer Society, Los Alamitos, CA, USA, 17059–17068. <https://doi.org/10.1109/CVPR52729.2023.01636>

Xiaoxiao Long, Cheng Lin, Lingjie Liu, Yuan Liu, Peng Wang, Christian Theobalt, Taku Komura, and Wenzheng Wang. 2023. Neuraludf: Learning unsigned distance fields for multi-view reconstruction of surfaces with arbitrary topologies. In *Proceedings of the IEEE/CVF Conference on Computer Vision and Pattern Recognition*. 20834–20843.

William E. Lorensen and Harvey E. Cline. 1987. Marching cubes: A high resolution 3D surface construction algorithm. In *Proceedings of the 14th Annual Conference on Computer Graphics and Interactive Techniques (SIGGRAPH '87)*. Association for Computing Machinery, New York, NY, USA, 163–169. <https://doi.org/10.1145/37401.37422>

Daniel Maturana and Sebastian Scherer. 2015. VoxNet: A 3D Convolutional Neural Network for real-time object recognition. In *2015 IEEE/RSJ International Conference on Intelligent Robots and Systems (IROS)*. 922–928. <https://doi.org/10.1109/IROS.2015.7353481>

- Lars Mescheder, Michael Oechsle, Michael Niemeyer, Sebastian Nowozin, and Andreas Geiger. 2019. Occupancy Networks: Learning 3D Reconstruction in Function Space. In *Proceedings of the IEEE/CVF Conference on Computer Vision and Pattern Recognition (CVPR)*.
- Ben Mildenhall, Pratul P Srinivasan, Matthew Tancik, Jonathan T Barron, Ravi Ramamoorthi, and Ren Ng. 2021. Nerf: Representing scenes as neural radiance fields for view synthesis. *Commun. ACM* 65, 1 (2021), 99–106.
- Sehee Min, Jaedong Lee, Jungdam Won, and Jehee Lee. 2017. Soft shadow art. In *Proceedings of the Symposium on Computational Aesthetics* (Los Angeles, California) (CAE '17). Association for Computing Machinery, New York, NY, USA, Article 3, 9 pages. <https://doi.org/10.1145/3092912.3092915>
- Niloy J. Mitra and Mark Pauly. 2009. Shadow art. In *ACM SIGGRAPH Asia 2009 Papers* (Yokohama, Japan) (SIGGRAPH Asia '09). Association for Computing Machinery, New York, NY, USA, Article 156, 7 pages. <https://doi.org/10.1145/1661412.1618502>
- Jeong Joon Park, Peter R. Florence, Julian Straub, Richard A. Newcombe, and S. Lovegrove. 2019. DeepSDF: Learning Continuous Signed Distance Functions for Shape Representation. *2019 IEEE/CVF Conference on Computer Vision and Pattern Recognition (CVPR)* (2019), 165–174. <https://api.semanticscholar.org/CorpusID:58007025>
- C. Qi, L. Yi, Hao Su, and Leonidas J. Guibas. 2017. PointNet++: Deep Hierarchical Feature Learning on Point Sets in a Metric Space. In *Neural Information Processing Systems*. <https://api.semanticscholar.org/CorpusID:1745976>
- Charles Ruizhongtai Qi, Hao Su, Kaichun Mo, and Leonidas Guibas. 2016. PointNet: Deep Learning on Point Sets for 3D Classification and Segmentation. (12 2016).
- Kaustubh Sadekar, Ashish Tiwari, and Shanmuganathan Raman. 2022. Shadow Art Revisited: A Differentiable Rendering Based Approach. In *Proceedings of the IEEE/CVF Winter Conference on Applications of Computer Vision (WACV)*. 29–37.
- Silvio Savarese, Marco Andreetto, Holly Rushmeier, Fausto Bernardini, and Pietro Perona. 2007. 3d reconstruction by shadow carving: Theory and practical evaluation. *International journal of computer vision* 71 (2007), 305–336.
- Yuliy Schwartzburg and Mark Pauly. 2012. *Design and Optimization of Orthogonally Intersecting Planar Surfaces*. 191–199. https://doi.org/10.1007/978-3-642-23435-4_22
- Steven A Shafer and Takeo Kanade. 1983. Using shadows in finding surface orientations. *Computer Vision, Graphics, and Image Processing* 22, 1 (1983), 145–176. [https://doi.org/10.1016/0734-189X\(83\)90099-3](https://doi.org/10.1016/0734-189X(83)90099-3)
- Abhishek Sharma, Oliver Grau, and Mario Fritz. 2016. VConv-DAE: Deep Volumetric Shape Learning Without Object Labels. (04 2016). https://doi.org/10.1007/978-3-319-49409-8_20
- Maxim Tatarchenko, Alexey Dosovitskiy, and Thomas Brox. 2017. Octree Generating Networks: Efficient Convolutional Architectures for High-resolution 3D Outputs. 2107–2115. <https://doi.org/10.1109/ICCV.2017.230>
- Kushagra Tiwary, Tzofi Klinghoffer, and Ramesh Raskar. 2022. Towards learning neural representations from shadows. In *European Conference on Computer Vision*. Springer, 300–316.
- Kenji Tojo, Ariel Shamir, Bernd Bickel, and Nobuyuki Umetani. 2024. Fabricable 3D Wire Art. In *ACM SIGGRAPH 2024 Conference Papers* (Denver, CO, USA) (SIGGRAPH '24). Association for Computing Machinery, New York, NY, USA, Article 134, 11 pages. <https://doi.org/10.1145/3641519.3657453>
- David L Waltz. 1975. Understanding line drawings of scenes with shadows. *The psychology of computer vision* (1975), 19–91.
- Peng Wang, Lingjie Liu, Yuan Liu, Christian Theobalt, Taku Komura, and Wenping Wang. 2021. Neus: Learning neural implicit surfaces by volume rendering for multi-view reconstruction. *arXiv preprint arXiv:2106.10689* (2021).
- Kang Wu, Xiaoming Fu, Renjie Chen, and Ligang Liu. 2022. Survey on computational 3D visual optical art design. *Visual Computing for Industry, Biomedicine, and Art* 5 (2022). <https://api.semanticscholar.org/CorpusID:254876286>
- Zhirong Wu, Shuran Song, Aditya Khosla, Fisher Yu, Linguang Zhang, Xiaoou Tang, and Jianxiong Xiao. 2015. 3D ShapeNets: A deep representation for volumetric shapes. In *2015 IEEE Conference on Computer Vision and Pattern Recognition (CVPR)*. 1912–1920. <https://doi.org/10.1109/CVPR.2015.7298801>
- Yaoqing Yang, Chen Feng, Yiru Shen, and Dong Tian. 2018. FoldingNet: Point Cloud Auto-Encoder via Deep Grid Deformation. 206–215. <https://doi.org/10.1109/CVPR.2018.00029>